A geometry-based model describes lumen stability in epithelial cells

Claudia G. Vasquez[1,3], Vipul T. Vachharajani[2,3], Carlos Garzon-Coral[1], and Alexander R. Dunn[1,2*]
[1]Department of Chemical Engineering, [2]Biophysics Program
Stanford University, Stanford CA 94305 USA
[3]These authors contributed equally to this work.
*Corresponding author.

Abstract
A continuous sheet of epithelial cells surrounding a hollow opening, or lumen, defines the basic topology of numerous organs. *De novo* lumen formation is a central feature of embryonic development whose dysregulation leads to congenital and acquired diseases of the kidney and other organs. While prior work has described the hydrostatic pressure-driven expansion of lumens when they are large, the physical mechanisms that promote the formation and maintenance of small, nascent lumens are less explored. In particular, models that rely solely on pressure-driven expansion face a potential challenge in that the Laplace pressure, which resists lumen expansion, is predicted to scale inversely with lumen radius. We investigated the cellular and physical mechanisms responsible for stabilizing the initial stages of lumen growth using a 3D culture system in which epithelial cells spontaneously form hollow lumens. Our experiments revealed that neither the actomyosin nor microtubule cytoskeletons are required to stabilize lumen geometry, and that a positive intraluminal pressure is not necessary for lumen stability. Instead, our observations are in agreement with a quantitative model in which cells maintain lumen shape due to topological and geometrical factors tied to the establishment of apico-basolateral polarity. We suggest that this model may provide a general physical mechanism for the formation of luminal openings in a variety of physiological contexts.

Introduction

Lumens, or hollow openings surrounded by sheets of cells, are a ubiquitous structural feature of metazoans. While the molecular components required for lumen formation have been characterized in some in detail, the physical mechanisms that underlie the initial steps in lumen formation remain less explored (Bryant et al., 2010; Cerruti et al., 2013; Ferrari et al., 2008; Martín-Belmonte et al., 2008; O'Brien et al., 2001; Odenwald et al., 2017; Rodríguez-Fraticelli et al., 2010; Sigurbjörnsdóttir et al., 2014; Wang et al., 1990). In particular, how lumen shape is stabilized when luminal volume is small is not well understood.

Here we examine the mechanics of lumen formation and expansion in Madin Darby Canine Kidney (MDCK) cell spheroids, an archetypal cell culture model for studying lumenogenesis. Previous work in MDCK spheroids and other systems has assumed that lumen growth is driven by hydrostatic pressure (Fig. 1a) (Chan et al., 2019; Dasgupta et al., 2018; Latorre et al., 2018; Ruiz-Herrero et al., 2017). In this model, lumen growth is governed by the Young-Laplace equation, which states that the pressure difference (***P***) between the cells and the lumen is counterbalanced by the surface tension (γ) of the lumen surface (apical faces of the cells) and inversely proportional to the lumen radius (***r***): $\Delta P = \frac{2\gamma}{r}$. The presence of a pressure gradient is motivated by work that showed that ion channels are critical for lumen formation and expansion *in vitro* and *in vivo* (Bagnat et al., 2007; Yap et al., 1993), and by pressure-driven fluctuations in lumen size in some model systems (Chan et al., 2019; Ruiz-Herrero et al., 2017). Importantly, this model predicts that lumen shape must be close to spherical.

For large lumens (10-100 μm in radius) the predicted Laplace pressure required for stability is ~50-100 Pa, in line with previously published luminal pressures (Latorre et al., 2018) (Fig. 1a). However, for lumens of ~1 μm in radius, the hydrostatic pressure required to drive lumen expansion is on the order of 10-100 kPa given an effective surface tension of given 10-100 mN m^{-1} (Andreucci et al., 1971; Daily et al., 1984) (Fig. 1a). The inferred requirement for high pressures poses a potentially extreme physical challenge for cells to overcome during *de novo* lumen formation. We therefore sought to understand how cells might avoid this 'Laplace paradox' in the context of *de novo* lumen formation. In the following sections, we combine experiment and quantitative modeling to understand the physical mechanisms that dictate shape and stability for small (2-4 cells), intermediate (5-8 cells), and large (>8 cells) lumens.

Lumen shapes for small- and intermediate-size MDCK spheroids are inconsistent with a Laplace model of lumen stability

We seeded MDCK cells expressing a fluorescent marker for actin filaments (Lifeact-RFP) in the recombinant extracellular matrix Matrigel. Under these culture conditions, MDCK cells spontaneously form hollow spheroids within 24 hours. To obtain high-resolution images of nascent lumens, we imaged young (18-24 hours) spheroids using lattice light sheet microscopy (LLSM). This acquisition method produced images in which the two opposing apical cortices of the lumen are clearly distinguishable and separated by ~200-300 nm (Fig. 1b,c). We infer that cellular apical surfaces are intrinsically non-adherent, as even small fluctuations in cell shape would allow apposing apical surfaces to contact and potentially adhere. This "non-stick" behavior may reflect the enrichment of negatively charged sialoglycoproteins such as

Podocalyxin and/or the active exclusion of cell adhesion proteins (e.g. E-cadherin) (Ferrari et al., 2008; Kerjaschki et al., 1984; Strilić et al., 2010; Wang et al., 1990).

Importantly, the large majority of lumens generated by two or three cells had irregular, non-spherical shapes (Fig. 1b,c, Supplementary Fig. 1a). This latter observation indicates that at the earliest stages, lumen shape is not stabilized exclusively by pressure, but by some other mechanism. As established in other studies with MDCK cells, large lumens (diameter ~30 μm) were round and close to spherical (Fig. 1d).

To derive further insight into the physical mechanisms that dictate the shape and stability of small and intermediate-sized lumens, we next used confocal microscopy to quantify the shapes of the luminal (apical) and outer (basal) surfaces of intermediate-size MDCK spheroids grown for 2 days in 3D conditions. If lumens were stabilized solely by hydrostatic pressure at this stage, we would expect them to be spherical. Instead, as with two- to three-cell spheroids, the lumens of intermediate-sized spheroids (8-20 cells) were irregular in shape (Fig. 2a-d, Supplementary Fig. 1c). This observation is consistent with published shapes of both MDCK (Bryant et al., 2010; Cerruti et al., 2013; Ferrari et al., 2008; O'Brien et al., 2001) and other lumens observed in intact organisms (Benhamouche-Trouillet et al., 2018; Hoijman et al., 2015; Oteiza et al., 2008; Shahbazi et al., 2016; Strilić et al., 2010; Wong et al., 2010), though the irregularity of shape was not previously commented upon or explored in detail.

To determine how similar or dissimilar lumen shapes were to spheres, we calculated the sphericity Ψ given by $\psi = \frac{\pi^{1/3}(6V)^{2/3}}{A}$ for lumen volume V and surface area A. This metric ranges from 0 (far from spherical) to 1 (exactly a sphere). The sphericity of lumens ranged from Ψ~0.70 to very far from spherical (Ψ~0.3) (Fig. 2e), values substantially less spherical than, for example, a cube (Ψ = 0.81). In addition, we computed the mean curvature (H) at each voxel of lumen surface, normalized by lumen volume. These measurements demonstrate that lumens, even those with sphericity greater than 0.65, have areas of negative mean curvature, where the negative value denotes concave (inward) bending (red; Fig. 2b,d, left). The fraction of the total lumen surface area with negative mean curvature varied from 0.1 to over 0.4 for lumens from spheroids with eight cells (Fig. 2f). In contrast, the sphericity and fraction concavity of the basal surfaces of the spheroids were close to 1 and 0, respectively (Fig 2e, Supplementary Fig. 1c). This latter observation is consistent with the idea that the individual cells, and by extension spheroids as a whole, were at positive pressures relative to the surrounding medium (Jiang and Sun, 2013).

In sum, our data are inconsistent with a model of positive luminal pressure as the driving mechanism to maintain the shape of small- and intermediate-sized lumens. Instead, we noted that the average luminal surface area per cell remained roughly constant for spheroids of 2 to >8 cells (Fig. 2g). Together, these observations suggest a lumen growth mechanism in which the apical surface area per cell is actively regulated, and apical surface area is added faster than the equivalent amounts of luminal volume, leading to the observed irregular lumen shapes (see Discussion).

Cells regulate both luminal pressure and surface area to define lumen size and shape

The failure of Laplace pressure alone to account for the presence of large regions of concavity for small- and medium-sized lumens led us to develop a more complete physical description of the forces that determine lumen shape and stability. To do so, we constructed a

quantitative model that could account for the curvature of the luminal domains of individual cells (Fig. 3a). Inspired by a theoretical framework originally developed to explain the shape of red blood cells (Deuling and Helfrich, 1976), we developed a model that that incorporates the energetic contributions from the bending (effective bending modulus) and stretching of the apical domains (effective surface energy) of individual cells, in addition to lumen pressure.

As expected, versions of this model containing contributions from only membrane surface energy and pressure failed to account for our observations, as they either result in spherical lumens, or lumens that are not physically stable (see Supplementary Discussion). Instead, we considered scenarios in which lumen shape reflects a counterbalance of either *i*) bending and surface energies, or *ii*) bending energy and pressure. In the first scenario, lumen shape is analogous to a water balloon, where volume is constant and shape is determined by the energetic costs of apical surface bending vs. stretching (Fig. 3b, Supplementary Fig. 2a, b). In the second scenario, lumen shape is analogous to a partially inflated paper bag, such that surface area is constant and shape is determined by the relative costs of adding volume (i.e. pressure) vs. apical surface bending (Fig. 3c, Supplementary Fig. 2c,d). In both of these scenarios, decreasing the bending rigidity κ five-fold predicted that the shape of lumen-facing apical domains would become more extreme, i.e. convex lumens become more convex and concave lumens became more concave (Fig. 3b, c, Supplementary Fig. 3).

Drawing on previous work (Simson et al., 1998), we experimentally decreased apical surface bending energy with a cocktail of inhibitors (1 μM latrunculin A, 20 μM ML-7, 20 μM Y-27632, and 50 μM nocodazole) that works to acutely ablate the actomyosin and microtubule cytoskeletons (Owen et al., 2017) (Supplementary Video 1). Remarkably, lumen face shapes were largely unaffected by cytoskeletal ablation (Fig. 3e-h), with no significant change in surface area (Fig. 3i) and small increases, on average, in volume (Fig. 3j) and sphericity (Fig. 3k). Further, lumens with a high degree of concavity became modestly less concave after drug treatment (Fig. 3l), the opposite of what would be predicted by either the water balloon or paper bag scenarios (Fig. 3b, c). Our measurements are therefore inconsistent with scenarios in which lumen shape is determined by counterbalanced pairs of pressure, surface energy, and bending energy.

A third scenario, which we term a geometric frame, is that both luminal pressure and surface energy are both actively regulated. In this scenario the curvature of individual lumen faces is solely determined by the luminal pressure and surface energy, and is insensitive to changes in bending rigidity (Fig. 3d, Supplementary Fig. 3, Supplementary Discussion), consistent with our experimental observations (Fig. 3i-l). The requirements for the geometric frame scenario are plausible given that cells can actively regulate lumen pressure (Chan et al., 2019; Latorre et al., 2018) and luminal surface area (Fig. 2g). In addition, dual regulation of both pressure and surface area provides a straightforward means for cells to stabilize and grow lumens while maintaining both low pressures and surface energies (see Discussion). We conclude that, in this model system, cells regulate both lumen pressure and apical surface area in order to define lumen size and shape.

Luminal membrane specification can explain lumen geometry

The observations above led us to conclude that the shapes of lumens in spheroids composed 4-12 cells were dictated by the framework imposed by apical cell-cell contacts.

Therefore, we next considered what factors might dictate the geometry of apical contacts in intermediate-sized spheroids. One possibility was that the geometry of the cell-cell contacts might be determined primarily by the position of cells within the spheroid (Fig. 4a). To formalize this intuition, we considered a one-parameter model in which spheroid and lumen geometries are described by a random Voronoi tessellation of a ball (Fig. 4b). Briefly, 8-cell spheroids were modeled by placing 8 seed points at random within a unit ball. Each seed point generated a cell, where the interior of that cell corresponds to the set of points closest to a randomly placed seed point. For each cell, we classified each face as apical, basal, or lateral, and calculated the total lumen surface area from the sum of the apical faces (Fig. 4b, green). Because the lumen accounts for a small (<5%) fraction of the total spheroid volume at this early stage, the volume of the lumen was not explicitly modeled. This packing model does not account for the curved shapes of individual cellular apical domains, but it can capture the relation between cell packing and lumen size and geometry. The packing model produced a distribution of lumen surface areas in quantitative agreement with our experimental data of all lumens from 8-cell spheroids, including those treated with DMSO-vehicle control and cytoskeletal inhibitors (Fig. 4c). This result supports the notion that the specification of luminal membrane from cell-packing considerations is sufficient to largely account for lumen geometry in intermediate-sized spheroids.

Size-dependent crossover from irregular to spherical lumens

To directly test if modulating intraluminal pressure affects lumen shape, we treated MDCK spheroids grown in Matrigel for 3 days and 7 days with small molecules that act to promote or inhibit apical fluid secretion, the V2 receptor agonist 1-desamino-8-D-AVP (ddAVP, 10μM) (Grant et al., 1991) and the Na^+/K^+ ATPase inhibitor ouabain (330 μM) (Chan et al., 2019; Schoner, 2002), respectively. Treatment of MDCK spheroids either ddAVP or ouabain for 4 hours caused lumen cross-sectional area to increase (Fig. 4e, Supplementary Fig. 4a) compared to vehicle controls while having little change in cell thickness (Fig. 4f, Supplementary Fig. 4b). However, neither of these treatments caused lumens to become rounder. The isoperimetric quotient is the 2-D measurement analogous to sphericity, where a value of 1 describes a perfect circle. The isoperimetric quotient of lumen cross-sections did not change significantly upon treatment with either drug (Fig. 4g, Supplementary Fig. 4c). Thus, for intermediate-sized lumens, modulated pressure did not strongly influence lumen shape.

Instead, we observed an abrupt crossover from irregular to spherical lumen morphology as lumens grew in size. Following a prolonged phase of irregular growth, the lumens of large MDCK spheroids, with an estimated radius of ~10 μm and tens of cells, tended towards spherical geometries (Fig. 4h). A straightforward explanation is that as the spheroid increases in size, the osmotic pressure required to deform the enclosing monolayer should scale inversely as the spheroid radius per Laplace's law. Thus, there is a spheroid radius beyond which this pressure difference is sufficient to yield approximately spherical lumens (Fig. 4i). These results are in good agreement with recent work that measured the luminal pressure of large MDCK domes as 60-80 Pa (Latorre et al., 2018), which is predicted to lead to round lumens for radii greater than 30 μm. For different cell types and tissues, different combinations of bending moduli and luminal pressures likely set the transition to round lumens at different critical radii (Fig. 4i).

Discussion

A fundamental challenge for *de novo* lumen growth is to either overcome or circumvent the high hydrostatic pressures dictated by the Young-Laplace law when lumens are small. Our data indicate that pressure does not play a dominant role in stabilizing small lumens (Fig. 3e-l, Fig. 4d-f). Instead, in our model system, early stages of lumen growth appear to be accomplished by the simple addition of a roughly constant amount (Fig. 2g) of luminal membrane per cell, with sufficient fluid transport to allow the lumen to gradually increase in volume while avoiding large positive or negative pressures. Consistent with this understanding, the geometries of intermediate-sized lumens, as parametrized by the ratio of surface area to volume, could be described by a simple geometric model based on the positions of individual cell nuclei (Fig. 4b,c). Our findings thus highlight a pressure-independent method for stabilizing lumens that, to our knowledge, has been largely overlooked despite its possible prevalence (Alvers et al., 2014; Gao et al., 2017; Shahbazi et al., 2016).

The advantages of pressure-independent lumen growth remain to be firmly established in an *in vivo* context. However, we note that this mechanism is predicted to be physically robust and energy efficient relative to pressure-driven growth, which exposes tissues to pressure-driven rupture (Chan et al., 2019; Ruiz-Herrero et al., 2017). Notably, cells in some model systems continue to utilize pressure-independent mechanisms to grow lumens beyond these intermediate stages, for example, by addition of cells or by fusion of smaller lumens (Cerruti et al., 2013; Dumortier et al., 2019). Importantly, when lumens achieve a sufficient diameter, a pressure-driven transition to circular cross-sections will dominate, providing a simple way to generate regular, space-filling shapes like spheres and tubes (Lubarsky and Krasnow, 2003). Pressure-dependent and pressure-independent mechanisms for dictating lumen shape thus coexist and fulfill complementary functions in driving embryonic growth and tissue morphogenesis.

Previous work demonstrates that the establishment of apical-basolateral polarity and the earliest stages in lumen formation are tightly coupled at a molecular level (Bryant et al., 2010; Bryant and Mostov, 2008; O'Brien et al., 2001; Sigurbjörnsdóttir et al., 2014). Our work builds on these observations, and highlights the deep connections between the establishment of a distinct, lumen-facing apical membrane and the physical mechanisms that stabilize small lumens (e.g Fig. 2g). Evolutionary data indicate the molecular components required for the establishment of a defined apical domain are ancient, and appeared simultaneously with the advent of multicellular animals (Belahbib et al., 2018). It is intriguing to speculate that this mechanism for shaping tissues may represent an important, enabling advance in the appearance of complex, multicellular life.

Acknowledgements

C.G.V. is supported by the NIH NIGMS (1F32GM125113-01). V.T.V. is supported by the Stanford Medical Scientist Training Program (NIH T32GM007365). C.G.C is supported by a long-term postdoctoral fellowship from the Human Frontier Science Program. A.R.D. acknowledges the HHMI (Faculty Scholar Award), and the NIH (R01GM117457, R35GM130332). We want to thank Dr. Christina Hueschen, other members of the Dunn lab, and Dr. Lucy E. O'Brien for discussion and insightful comments on the manuscript.

Author contributions

C.G.V., V.T.V, and C.G.C. performed experiments and analyzed data. V.T.V developed the models with input from C.G.V. and A.R.D. All authors wrote and edited the manuscript.

Methods

Cells culture and generation of cell lines. MDCK II cells were cultured at 37 ºC and 5% CO_2 in DMEM (Thermo Fisher Cat. #11885076) supplemented with 10% fetal bovine serum (FBS, Corning) and 1% penicillin-streptomycin (ThermoFisher). Live-cell confocal and brightfield microscopy experiments were performed in Leibovitz's L15 media (L15, ThermoFisher) supplemented with 10% FBS (Corning) and 1% penicillin-streptomycin. Live-cell lattice light sheet microscopy was performed in L15 media supplemented with 1% FBS and Insulin-Transferrin-Selenium (Invitrogen). MDCK cells constitutively expressing Lifeact-RFP were generated to visualize the actin cytoskeleton. Briefly, cells were transfected with a plasmid containing the PiggyBac transposon system and the Lifeact-RFP sequence (DNA2.0), cells were selected for plasmid integration with geneticin (G418, ThermoFisher).

Generating MDCK spheroids. MDCK spheroid were generated as previously described in (Peterman and Prekeris, 2017; Vieira et al., 2006). Briefly, 75 µL of cell suspension containing ~10^4 cells were mixed with 150 µL Matrigel GFR (Corning CB-40230). 25 µL drops of cell-Matrigel suspensions were seeded into each well of an 8-well chambered coverglass (Nunc, No. 1.5) and incubated at 37 ºC for 30 minutes before adding DMEM to cells. Media was changed every other day. At least 2 hours prior to live-imaging experiments, media was changed to L15.

Pharmacological inhibition experiments. To perturb the actomyosin and microtubule cytoskeletons, cells were treated with a cytoskeletal inhibitor cocktail composed of latrunculin A (Sigma, 1 µM), Rho-kinase inhibitor Y-27632 (STEMCELL Technologies, 20 µM), MLCK inhibitor ML-7 (Enzo, 20 µM), and nocodazole (Sigma, 50µM). The cytoskeletal inhibitor cocktail was made at 5X final concentration in L15 media and 100 µL were added to imaging well with 400 µL of L15. To disrupt ion and fluid pumping, spheroids were treated with ouabain, a Na^+/K^+ ATPase inhibitor (Sigma) or 1-deamino-8-D-arginine vasopressin (ddAVP, Sigma), a vasopressin receptor agonist. Each was dissolved in distilled water at 1000X final concentration and diluted in cell culture media immediately before treatment for 4-24 hours before DIC imaging. Ouabain was used at a final concentration of 333 µM while ddAVP was used at a final concentration of 10 µM.

Cell immunofluorescence. MDCK cells were fixed with 4% paraformaldehyde in PBS for 15 min at room temperature. Samples were blocked and permeabilized in 0.1% Triton, 1% bovine serum albumin (BSA, Sigma) in PBS for 1 h at room temperature. Cells were incubated in primary antibody solution in 0.1% Triton, 1% BSA in PBS overnight at 4 ºC, and in secondary antibody solution in 0.1% Triton, 1% BSA in PBS for 2 hours at room temperature. To identify nuclei, Hoechst solution (Hoechst 34580, Invitrogen) was added at 1:1000 dilution to secondary antibody solution. To identify actin filaments phalloidin (ActinGreen 488 ReadyProbes, Invitrogen) was added at 1 drop/mL. Antibodies and corresponding concentrations used in this investigation are listed in Table S1. Images were acquired at room temperature (~22 ºC) using an inverted Zeiss LSM 780 confocal microscope with a 40X/1.3 NA C-Apo water objective, 405 nm diode laser, 488 nm argon laser, 561 nm diode laser, 633 nm HeNe laser, and a pinhole setting between 1 and 2 Airy Units. All images were acquired using Zen Black software (Carl Zeiss).

Table S1| Antibodies used and concentrations

Antibody	Dilution	Source
rabbit anti-Tight Junction Protein1 (ZO-1)	1:1000	Novus Biologicals (NBP1-85046)
goat anti-rabbit IgG Alexa Fluor 647	1:1000	Cell Signaling Technology (Cat. 4414)

Lattice light sheet microscopy. We used a custom-built lattice light sheet microscope (LLSM) (Chen et al., 2014) to image MDCK spheroids. Spheroids were grown in 3 µL droplets of Matrigel without Phenol red (Corning) seeded on top of a 5 mm round cover glass (Warner Instruments). The samples were incubated for 12-36 hours at 37 °C in 25 mm tissue culture plates. Before experiments, samples were transferred to LLSM imaging medium (L15 media supplemented with 1% FBS and Insulin-Transferrin-Selenium Invitrogen) for 12-16 hours.

Samples were illuminated by a 561 nm diode laser (0.5W, Coherent) using an excitation objective (Special Optics, 0.65 NA with a working distance of 3.74-mm) at 2% AOTF transmittance and laser power of 100 mW. Order transfer functions were obtained empirically by acquiring point-spread functions using 200-nm TetraSpeck beads adhered freshly to 5-mm glass coverslips (Invitrogen T7280) for each wavelength and for each day of experiments.

To achieve structured illumination, a square lattice was displayed on a spatial light modulator. This lattice was generated by an interference pattern of 59 Bessel beams separated by 1.67 µm and cropped to 0.22 with a 0.325 inner NA and 0.40 outer NA. The lattice light sheet was dithered 25 µm to obtain homogeneous illumination with 5% flyback time. Fluorescent signal was collected by a Nikon detection objective (CFI Apo LWD 25XW, 1.1 NA, 2-mm working distance), coupled with a 500 mm focal length tube lens (Thorlabs), a Semrock filter (BL02-561R-25) and sCMOS cameras (Hamamatsu Orca Flash 4.0 v2) with a 103 nm/pixel magnification.

Z-Stacks were acquired by moving the lattice light sheet and the detection objective synchronously, using a galvo mirror coupled at the back focal plane of the illumination objective and a piezomotor, respectively. The slices of the stacks were taken with an interval of 100 nm through ranges of 30-35 μm at 100ms camera exposure with 1-5 second intervals between z-stacks.

Raw data was flash corrected (Liu et al., 2017) and deconvolved using an iterative Richardson-Lucy algorithm (Chen et al., 2014) run on two graphics processing units (NVIDIA, GeForce GTX TITAN 4Gb RAM). Flash calibration, flash correction, channel registration, order transfer function calculation and image deconvolution were done using the LLSpy open software (Lambert and Shao, 2019). Visualization of the images and volume inspection were done using Spimagine (https://github.com/maweigert/spimagine) and ClearVolume (Royer et al., 2015).

Confocal microscopy. All live confocal images were acquired at 37 ºC using an inverted Zeiss LSM 780 confocal microscope with a 40X/1.3 NA C-Apo water objective, 561 nm diode laser, and a pinhole setting between 1 and 2 Airy Units. All images were acquired using Zen Black software (Carl Zeiss).

Differential interference contrast (DIC) microscopy. DIC microscopy was performed at 37ºC using a Nikon Ti-E inverted microscope with a 20X/0.5 NA Plan Fluor CFI objective and N2 DIC prisms. Image acquisition was controlled using micromanager software (Edelstein et al., 2014).

Confocal image analysis. A Fiji (Schindelin et al., 2012) plugin was used to correct 3D drift in all live-cell confocal images (Parslow et al., 2014; Schindelin et al., 2012).

Cell number. The number of cells in each spheroid were manually and independently determined by CGV and VTV using the Lifeact-RFP signal to determine cell-cell boundaries.

Segmentation and surface shape calculations. Custom-developed Python code was used to detect and segment the lumens (i.e. apical surface) and basal surfaces spheroids. Briefly, lumen and basal surface boundaries were detected in each slice from segmented images using OpenCV. The boundary was parameterized by contour length. *X*- and *Y*-coordinates of each boundary were fit to Fourier series of varying order up to 15 (Schmittbuhl et al., 2003). A Bayesian Information Criterion was used to select the Fourier order to minimize overfitting (Neath and Cavanaugh, 2012). The smoothed boundary was used for calculations of local curvature, volume, and surface area. From these calculations sphericity (Ψ) was computed as:

$$\Psi = \frac{\pi^{\frac{1}{3}}(6V)^{\frac{2}{3}}}{A}$$

Where ***V*** is surface volume, and ***A*** is surface area.

Estimated lumen radius was calculated from the lumen volume as:

$$r = \left(\frac{3V}{4\pi}\right)^{\frac{1}{3}}$$

Where ***V*** is lumen volume.

Mean curvature. For each voxel on a surface, the smoothed contours in *XY* and *YZ* correspond to 1-dimensional curves on the surface, which are orthogonal at that voxel. The curvatures of these curves were computed using the Fourier representation. From these two curves, the surface mean curvature was estimated as follows: The surface normal vector was estimated as the cross product of the unit tangent vectors to each of these orthogonal cross-sectional curves. Because these two cross-sections are orthogonal, this is an appropriate approximation.
Let a cross-section contour be given by $\underline{\gamma}(s)$. The Frenet-Serret formula gives $\vec{T}'(s) = k\vec{N}$, where $\vec{T}$and $\vec{N}$ are the unit normal and binormal vectors of the contour, respectively. The curvature can be related to the geodesic (k_g) and normal (k_n) curvatures by the formula $\vec{T}'(s) = k_g\vec{t} + k_n\vec{u}$, where $\vec{u}$ is the surface unit normal vectors, and $\vec{t} = \vec{u} \times \vec{T}$, which also follows from the Frenet-Serret formula (Gray, 1997). The normal curvatures of each cross-sectional curve were thus computed from the estimated surface normal vector and the Frenet-Serret normal vector of that curve as $k_n = k\vec{N} \cdot \vec{u}$. The mean curvature was then calculated as the mean of the two orthogonal normal curvatures.

Determination of fraction concave surface. Each segmented surface (lumen or basal surface) has a distribution of mean curvatures. To calculate the fraction concave surface area, we determined what fraction of each surface had negative (concave) mean curvatures.

DIC image analysis. For each spheroid imaged in DIC, the apical (lumen) and basal surfaces were traced manually in Fiji (Schindelin et al., 2012) using the polygon selection tool. For apical (***a***) and basal (***b***) surfaces, the enclosed area (***A***) and perimeter (***P***) were measured automatically in Fiji. Mean cell thickness was computed as:

$$\frac{2(A_b - A_a)}{P_b + P_a}$$

Isoperimetric quotient (IPQ) is an analogous measure to sphericity for 2-dimensionalshapes. IPQ was computed as:

$$IPQ = \frac{4\pi A_a}{P_a^2}$$

where an IPQ of 1 denotes a perfect circle.

Statistical analysis. Statistically significant differences between control and drug treatment groups were assessed via a Rank-sum test (Fig. 3i-l, Fig. 4d-f). Data comparing before and after treatment were assessed using the Paired Wilcoxon test (Fig. 3i-l). A 2-sample Kolmogorov-Smirnov test was used to compare the output of the Voronoi model to live-cell data distributions (Fig. 4c). All statistical analyses were performed using the stats module of the SciPy Python package.

Code availability. Python analysis procedures are available from the corresponding author upon request.

Data availability. All data generated or analyzed in this study are available from the corresponding author upon request.

References

Alvers, A. L., S. Ryan, P. J. Scherz, J. Huisken, and M. Bagnat, 2014, Single continuous lumen formation in the zebrafish gut is mediated by smoothened-dependent tissue remodeling: Development, v. 141, p. 1110-1119.

Andreucci, V. E., J. Herrera-Acosta, F. C. Rector, and D. W. Seldin, 1971, Effective glomerular filtration pressure and single nephron filtration rate during hydropenia, elevated ureteral pressure, and acute volume expansion with isotonic saline: J Clin Invest, v. 50, p. 2230-4.

Bagnat, M., I. D. Cheung, K. E. Mostov, and D. Y. Stainier, 2007, Genetic control of single lumen formation in the zebrafish gut: Nat Cell Biol, v. 9, p. 954-60.

Belahbib, H., E. Renard, S. Santini, C. Jourda, J. M. Claverie, C. Borchiellini, and A. Le Bivic, 2018, New genomic data and analyses challenge the traditional vision of animal epithelium evolution: BMC Genomics, v. 19, p. 393.

Benhamouche-Trouillet, S., E. O'Loughlin, C. H. Liu, W. Polacheck, J. Fitamant, M. McKee, N. El-Bardeesy, C. S. Chen, and A. I. McClatchey, 2018, Proliferation-independent role of NF2 (merlin) in limiting biliary morphogenesis: Development, v. 145.

Bryant, D. M., A. Datta, A. E. Rodríguez-Fraticelli, J. Peränen, F. Martín-Belmonte, and K. E. Mostov, 2010, A molecular network for de novo generation of the apical surface and lumen: Nature Publishing Group, v. 12, p. 1035-1045.

Bryant, D. M., and K. E. Mostov, 2008, From cells to organs: building polarized tissue: Nature reviews Molecular cell biology, v. 9, p. 887-901.

Cerruti, B., A. Puliafito, A. M. Shewan, W. Yu, A. N. Combes, M. H. Little, F. Chianale, L. Primo, G. Serini, K. E. Mostov, A. Celani, and A. Gamba, 2013, Polarity, cell division, and out-of-equilibrium dynamics control the growth of epithelial structures: Journal of Cell Biology, v. 203, p. 359-372.

Chan, C. J., M. Costanzo, T. Ruiz-Herrero, G. M. x. F. nke, R. J. Petrie, M. Bergert, A. D.-M. x. F. oz, L. Mahadevan, and T. Hiiragi, 2019, Hydraulic control of mammalian embryo size and cell fate: Nature, v. 96, p. 1-22.

Chen, B. C., W. R. Legant, K. Wang, L. Shao, D. E. Milkie, M. W. Davidson, C. Janetopoulos, X. S. Wu, J. A. Hammer, Z. Liu, B. P. English, Y. Mimori-Kiyosue, D. P. Romero, A. T. Ritter, J. Lippincott-Schwartz, L. Fritz-Laylin, R. D. Mullins, D. M. Mitchell, J. N. Bembenek, A. C. Reymann, R. Böhme, S. W. Grill, J. T. Wang, G. Seydoux, U. S. Tulu, D. P. Kiehart, and E. Betzig, 2014, Lattice light-sheet microscopy: imaging molecules to embryos at high spatiotemporal resolution: Science, v. 346, p. 1257998.

Daily, B., E. L. Elson, and G. I. Zahalak, 1984, Cell poking. Determination of the elastic area compressibility modulus of the erythrocyte membrane: Biophys J, v. 45, p. 671-82.

Dasgupta, S., K. Gupta, Y. Zhang, V. Viasnoff, and J. Prost, 2018, Physics of lumen growth: Proc Natl Acad Sci U S A, v. 115, p. E4751-E4757.

Deuling, H. J., and W. Helfrich, 1976, Red blood cell shapes as explained on the basis of curvature elasticity: Biophys J, v. 16, p. 861-8.

Dumortier, J. G., M. Le Verge-Serandour, A. F. Tortorelli, A. Mielke, L. de Plater, H. Turlier, and J. L. Maître, 2019, Hydraulic fracturing and active coarsening position the lumen of the mouse blastocyst: Science, v. 365, p. 465-468.

Edelstein, A. D., M. A. Tsuchida, N. Amodaj, H. Pinkard, R. D. Vale, and N. Stuurman, 2014, Advanced methods of microscope control using μManager software: J Biol Methods, v. 1.

Ferrari, A., A. Veligodskiy, U. Berge, M. S. Lucas, and R. Kroschewski, 2008, ROCK-mediated contractility, tight junctions and channels contribute to the conversion of a preapical patch into apical surface during isochoric lumen initiation: Journal of cell science, v. 121, p. 3649-3663.

Gao, L., Z. Yang, C. Hiremath, S. E. Zimmerman, B. Long, P. R. Brakeman, K. E. Mostov, D. M. Bryant, K. Luby-Phelps, and D. K. Marciano, 2017, Afadin orients cell division to position the tubule lumen in developing renal tubules: Development, v. 144, p. 3511-3520.
Grant, M. E., T. K. Neufeld, E. J. Cragoe, L. W. Welling, and J. J. Grantham, 1991, Arginine vasopressin stimulates net fluid secretion in a polarized subculture of cyst-forming MDCK cells: J Am Soc Nephrol, v. 2, p. 219-27.
Gray, m., 1997, Modern Differential Geometry of Curves and Surfaces with Mathematica, Second Edition: Textbooks in Mathematics, Taylor & Francis.
Hoijman, E., D. Rubbini, J. Colombelli, and B. Alsina, 2015, Mitotic cell rounding and epithelial thinning regulate lumen growth and shape: Nature Communications, v. 6, p. 7355.
Jiang, H., and S. X. Sun, 2013, Cellular pressure and volume regulation and implications for cell mechanics: Biophys J, v. 105, p. 609-19.
Kerjaschki, D., D. J. Sharkey, and M. G. Farquhar, 1984, Identification and characterization of podocalyxin--the major sialoprotein of the renal glomerular epithelial cell: J Cell Biol, v. 98, p. 1591-6.
Lambert, T., and L. Shao, 2019, tlambert03/LLSpy: v0.4.3x, Zenodo.
Latorre, E., S. Kale, L. Casares, M. G. x. F. m.-G. x. E. lez, M. Uroz, L. x. E. o. Valon, R. V. Nair, E. Garreta, N. Montserrat, A. x. E. n. Campo, B. Ladoux, M. Arroyo, and X. Trepat, 2018, Active superelasticity in three- dimensional epithelia of controlled shape: Nature Publishing Group, v. 563, p. 1-24.
Liu, S., M. J. Mlodzianoski, Z. Hu, Y. Ren, K. McElmurry, D. M. Suter, and F. Huang, 2017, sCMOS noise-correction algorithm for microscopy images: Nat Methods, v. 14, p. 760-761.
Lubarsky, B., and M. A. Krasnow, 2003, Tube morphogenesis: making and shaping biological tubes: Cell, v. 112, p. 19-28.
Martín-Belmonte, F., W. Yu, A. E. Rodríguez-Fraticelli, A. Ewald, Z. Werb, M. A. Alonso, and K. Mostov, 2008, Cell-Polarity Dynamics Controls the Mechanism of Lumen Formation in Epithelial Morphogenesis: Current Biology, v. 18, p. 507-513.
Neath, A., and J. Cavanaugh, 2012, The Bayesian information criterion: background, derivation, and applications: Wiley Interdisciplinary Reviews-Computational Statistics, v. 4, p. 199-203.
O'Brien, L. E., T. S. Jou, A. L. Pollack, Q. Zhang, S. H. Hansen, P. Yurchenco, and K. E. Mostov, 2001, Rac1 orientates epithelial apical polarity through effects on basolateral laminin assembly: Nature Cell Biology, v. 3, p. 831-838.
Odenwald, M. A., W. Choi, A. Buckley, N. Shashikanth, N. E. Joseph, Y. Wang, M. H. Warren, M. M. Buschmann, R. Pavlyuk, J. Hildebrand, B. Margolis, A. S. Fanning, and J. R. Turner, 2017, ZO-1 interactions with F-actin and occludin direct epithelial polarization and single lumen specification in 3D culture: Journal of cell science, v. 130, p. 243-259.
Oteiza, P., M. Koppen, M. L. Concha, and C. P. Heisenberg, 2008, Origin and shaping of the laterality organ in zebrafish: Development, v. 135, p. 2807-2813.
Owen, L. M., A. S. Adhikari, M. Patel, P. Grimmer, N. Leijnse, M. C. Kim, J. Notbohm, C. Franck, and A. R. Dunn, 2017, A cytoskeletal clutch mediates cellular force transmission in a soft, three-dimensional extracellular matrix: Mol Biol Cell, v. 28, p. 1959-1974.
Parslow, A., A. Cardona, and R. J. Bryson-Richardson, 2014, Sample drift correction following 4D confocal time-lapse imaging: J Vis Exp.
Peterman, E., and R. Prekeris, 2017, Understanding post-mitotic roles of the midbody during cell differentiation and polarization: Methods Cell Biol, v. 137, p. 173-186.
Rodríguez-Fraticelli, A. E., S. Vergarajauregui, D. J. Eastburn, A. Datta, M. A. Alonso, K. Mostov, and F. Martín-Belmonte, 2010, The Cdc42 GEF Intersectin 2 controls mitotic spindle orientation to form the lumen during epithelial morphogenesis: Journal of Cell Biology, v. 189, p. 725-738.

Royer, L. A., M. Weigert, U. Günther, N. Maghelli, F. Jug, I. F. Sbalzarini, and E. W. Myers, 2015, ClearVolume: open-source live 3D visualization for light-sheet microscopy: Nat Methods, v. 12, p. 480-1.
Ruiz-Herrero, T., K. Alessandri, B. V. Gurchenkov, P. Nassoy, and L. Mahadevan, 2017, Organ size control via hydraulically gated oscillations: Development, v. 144, p. 4422-4427.
Schindelin, J., I. Arganda-Carreras, E. Frise, V. Kaynig, M. Longair, T. Pietzsch, S. Preibisch, C. Rueden, S. Saalfeld, B. Schmid, J. Y. Tinevez, D. J. White, V. Hartenstein, K. Eliceiri, P. Tomancak, and A. Cardona, 2012, Fiji: an open-source platform for biological-image analysis: Nat Methods, v. 9, p. 676-82.
Schmittbuhl, M., B. Allenbach, J. Le Minor, and A. Schaaf, 2003, Elliptical descriptors: Some simplified morphometric parameters for the quantification of complex outlines: Mathematical Geology, v. 35, p. 853-871.
Schoner, W., 2002, Endogenous cardiac glycosides, a new class of steroid hormones: Eur J Biochem, v. 269, p. 2440-8.
Shahbazi, M. N., A. Jedrusik, S. Vuoristo, G. Recher, A. Hupalowska, V. Bolton, N. N. M. Fogarty, A. Campbell, L. Devito, D. Ilic, Y. Khalaf, K. K. Niakan, S. Fishel, and M. Zernicka-Goetz, 2016, Self-organization of the human embryo in the absence of maternal tissues: Nat Cell Biol, v. 18, p. 700-708.
Sigurbjörnsdóttir, S., R. Mathew, and M. Leptin, 2014, Molecular mechanisms of de novo lumen formation: Nat Rev Mol Cell Biol, v. 15, p. 665-76.
Simson, R., E. Wallraff, J. Faix, J. Niewöhner, G. Gerisch, and E. Sackmann, 1998, Membrane bending modulus and adhesion energy of wild-type and mutant cells of Dictyostelium lacking talin or cortexillins: Biophys J, v. 74, p. 514-22.
Strilić, B., J. Eglinger, M. Krieg, M. Zeeb, J. Axnick, P. Babál, D. J. Muller, and E. Lammert, 2010, Electrostatic Cell-Surface Repulsion Initiates Lumen Formation in Developing Blood Vessels: CURBIO, v. 20, p. 2003-2009.
Vieira, O. V., K. Gaus, P. Verkade, J. Fullekrug, W. L. Vaz, and K. Simons, 2006, FAPP2, cilium formation, and compartmentalization of the apical membrane in polarized Madin-Darby canine kidney (MDCK) cells: Proc Natl Acad Sci U S A, v. 103, p. 18556-61.
Wang, A. Z., G. K. Ojakian, and W. J. Nelson, 1990, Steps in the morphogenesis of a polarized epithelium. I. Uncoupling the roles of cell-cell and cell-substratum contact in establishing plasma membrane polarity in multicellular epithelial (MDCK) cysts: Journal of cell science, v. 95 (Pt 1), p. 137-151.
Wong, C. C., K. E. Loewke, N. L. Bossert, B. Behr, C. J. De Jonge, T. M. Baer, and R. A. R. Pera, 2010, Non-invasive imaging of human embryos before embryonic genome activation predicts development to the blastocyst stage: Nature Biotechnology, v. 28, p. 1115-1121.
Yap, A. S., J. W. Armstrong, E. J. Cragoe, J. R. Bourke, G. J. Huxham, and S. W. Manley, 1993, Activation of sodium transport mediates regulation of thyroid follicle volume in response to hypotonic media: Am J Physiol, v. 264, p. E644-9.

Figure 1

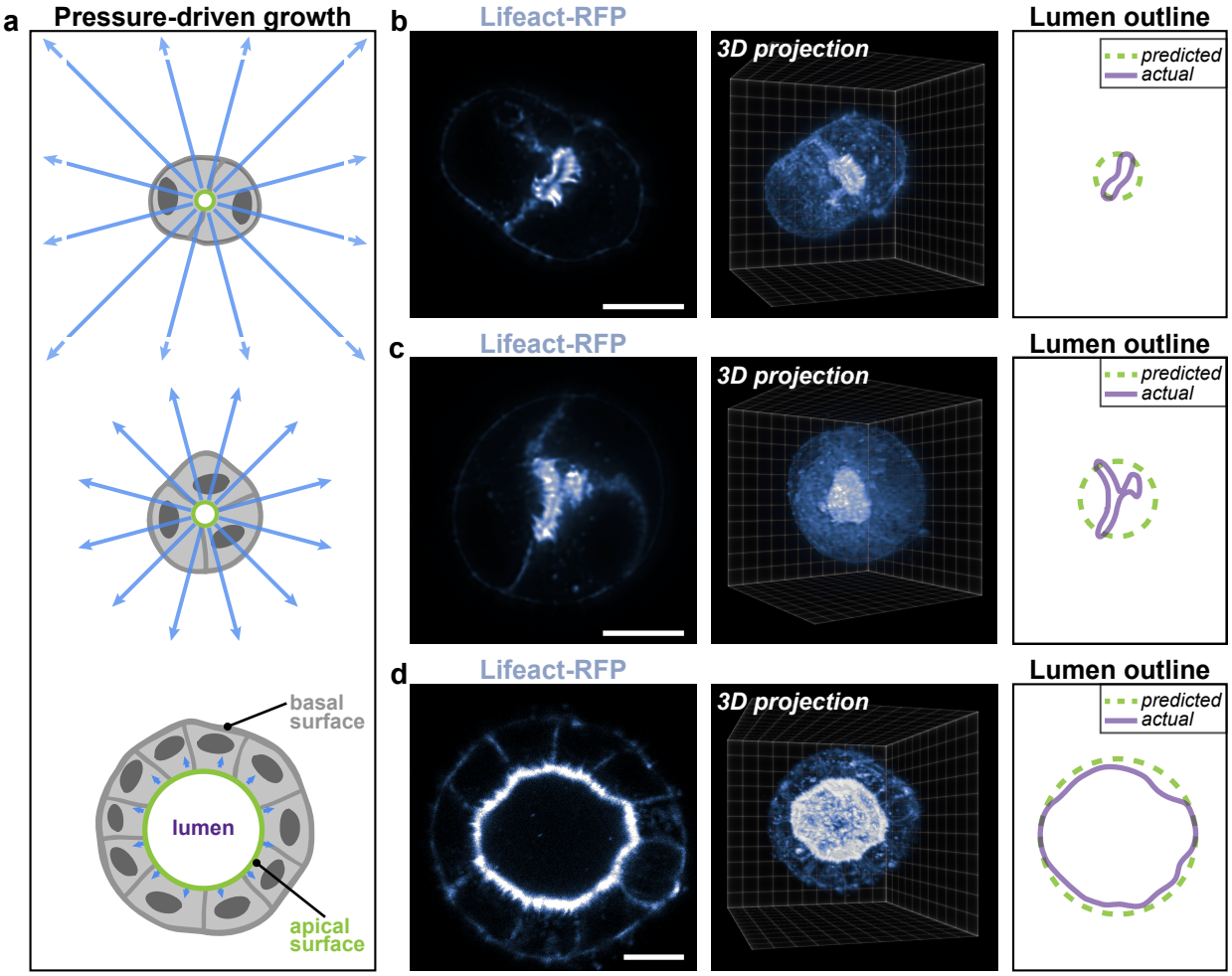

Figure 1 |Small lumens are irregular in shape. a, Schematic of lumen growth if governed by Young-Laplace equation. The pressure required to stabilize the lumen (blue arrows) is inversely proportional to the lumen radius. **b, c, d,** Representative images of two-, three-, and many-celled MDCK spheroids expressing Lifeact-RFP (F-actin marker) in a single plane (left) and in 3D-projection (middle) acquired on lattice light sheet microscope (**b,c**) and confocal microscope (**d**). Right panels show lumen shape predicted by a pressure-driven model (green) overlaid with actual lumen shape (purple). Scale bars are 10 μm.

Figure 2

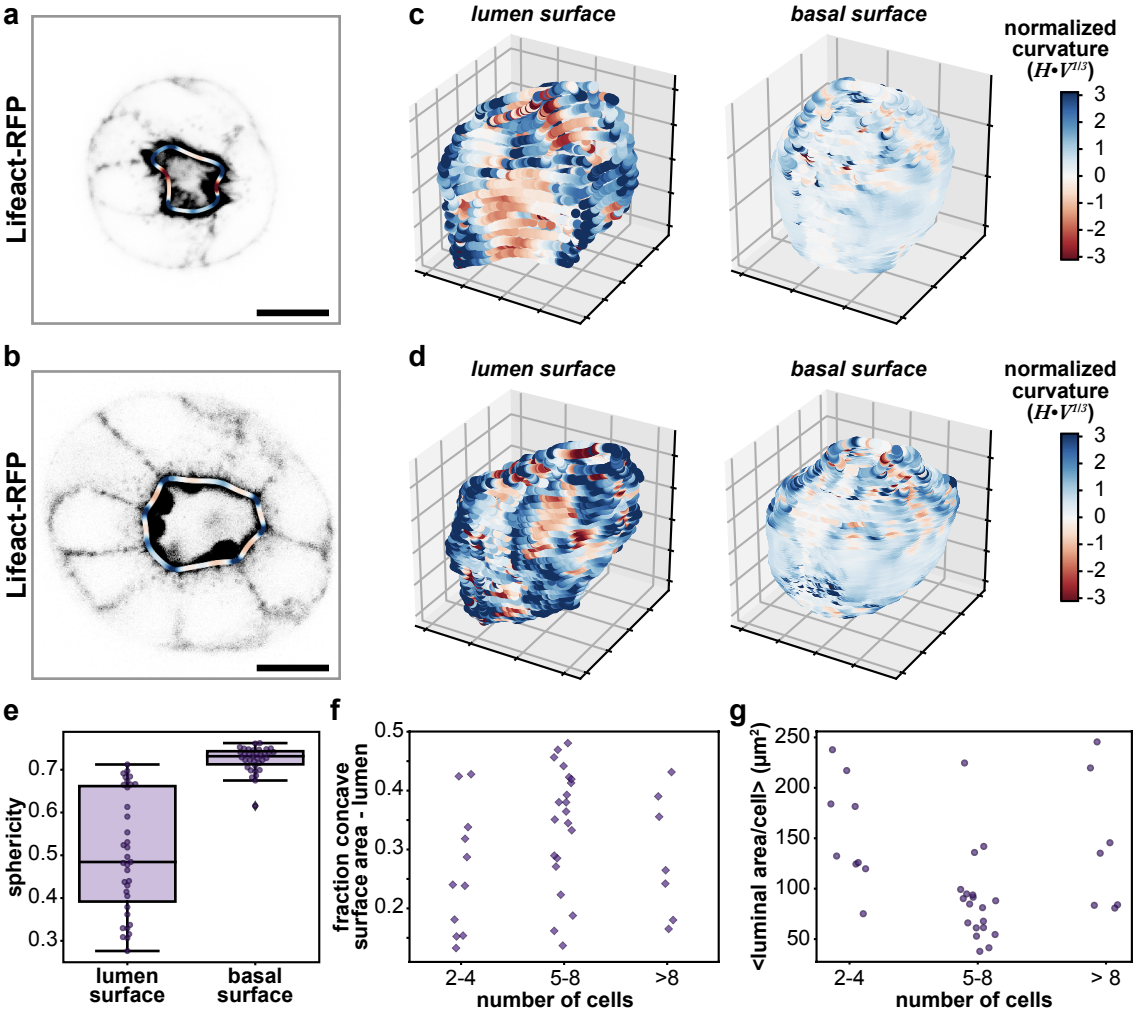

Figure 2 | Quantification of lumen morphology. a, b, Representative single-plane of two 2-day old MDCK spheroids expressing Lifeact-RFP (gray). The mean lumen curvature is superimposed as a red-blue outline, where red is concave (negative local curvature) and blue is convex (positive local curvature). **c,d,** 3D contour plots of lumen (left) and basal (right) surfaces showing local curvatures. **e,** Quantification of sphericity of the lumen and basal surfaces (N = 35 spheroids). **f,** Fraction of lumen surface that is concave (negative curvature) as a function of number of cells in the spheroid, **g,** Mean luminal surface area per cell plotted as a function of number of cells in the spheroid. Scale bars are 10 μm.

Figure 3

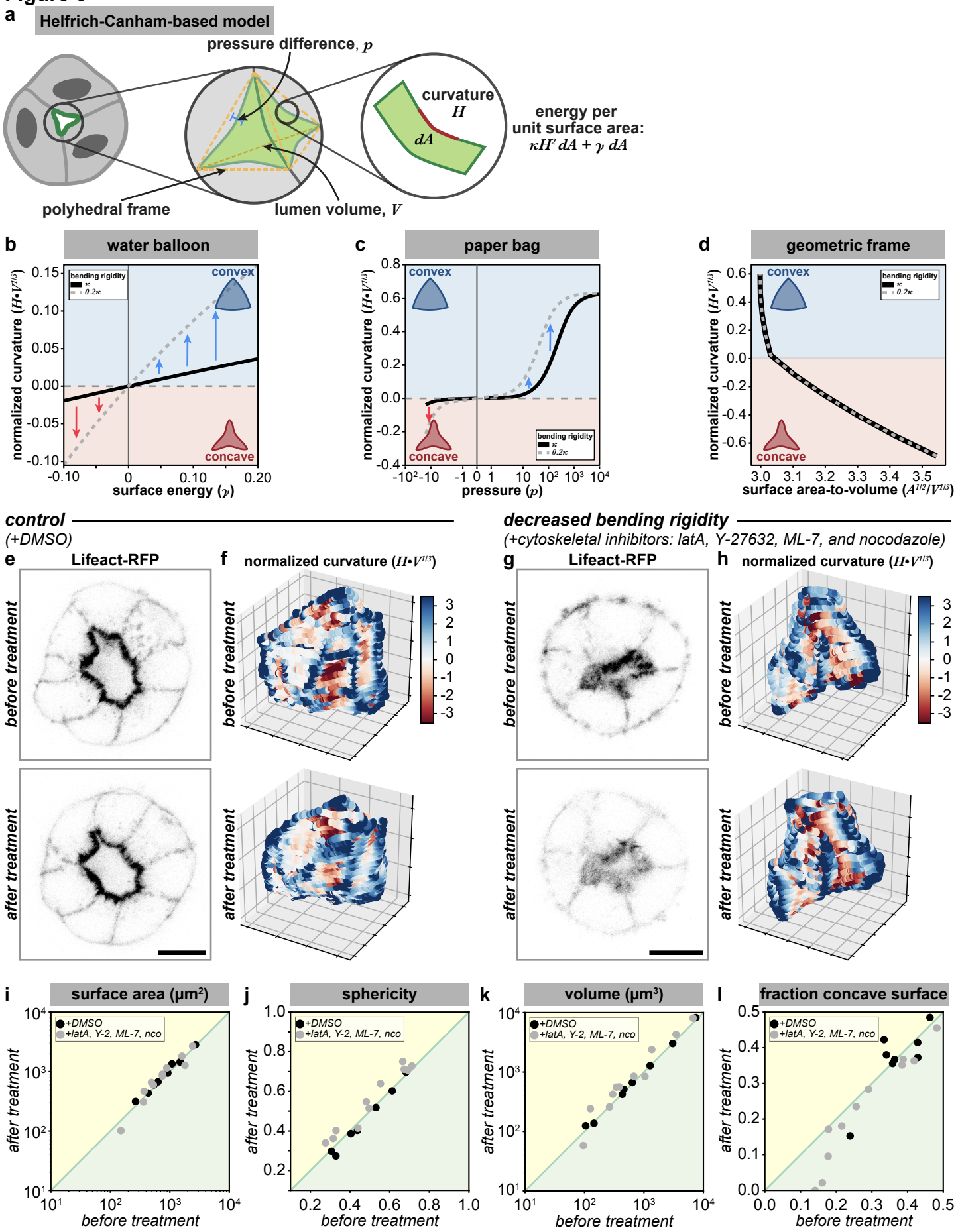
a
Helfrich-Canham-based model
pressure difference, p
curvature H
dA
energy per unit surface area: κH² dA + γ dA
polyhedral frame
lumen volume, V
b
water balloon
c
paper bag
d
geometric frame
normalized curvature (H•V^1/3)
surface energy (γ)
pressure (p)
surface area-to-volume (A^1/2/V^1/3)
convex
concave
bending rigidity
κ
0.2κ
control
(+DMSO)
decreased bending rigidity
(+cytoskeletal inhibitors: latA, Y-27632, ML-7, and nocodazole)
e
Lifeact-RFP
f
normalized curvature (H•V^1/3)
g
Lifeact-RFP
h
normalized curvature (H•V^1/3)
before treatment
after treatment
i
surface area (μm²)
j
sphericity
k
volume (μm³)
l
fraction concave surface
+DMSO
+latA, Y-2, ML-7, nco
after treatment
before treatment

Figure 3 | Acute cytoskeletal ablation does not significantly alter lumen shape. a, Schematic of a Helfrich-Canham based model of lumen shape that describes the curvature (***H***) of luminal faces via a surface energy (***γ***), luminal pressure (***p***), and a polyhedral frame (dotted orange line)(see text for details). **b-d**, Plots showing the effect of decreasing bending rigidity (***κ***) 5-fold (dotted grey line) on lumen face curvature ***H*** for cell-cell lumens in which (**b**) cells regulate only lumen volume (water balloon) (**c**) cells regulate only surface area (paper bag), or (**d**) in which cells regulate both pressure and surface area (geometric frame) all for octahedral lumen frames. **e**, Representative single-plane images and **f,** 3D contour plots of MDCK spheroids expressing Lifeact-RFP 2 min before (top) and 18 min after (bottom) addition of DMSO vehicle control. **g**, Representative single-plane images and **h,** 3D contour plots of MDCK spheroids expressing Lifeact-RFP 2 min before (top) and 18 min after (bottom) treatment with a cytoskeletal inhibitor cocktail (latrunculin A, Y-27632, ML-7, and nocodazole) to decrease bending rigidity (bottom). **i**, Log-log plot of lumen surface area before and after treatment (rank-sum test DMSO-cytoskeletal inhibitors $p = 0.41$, Wilcoxon signed rank test $t_{-2\ min}$-$t_{+18\ min}$(DMSO) $p = 0.069$, $t_{-2\ min}$-$t_{+18\ min}$(cytoskeletal inhibitors) $p = 0.091$). **j,** Log-log plot of lumen volume before and after treatment (rank-sum test DMSO-cytoskeletal inhibitors $p = 0.13$, Wilcoxon signed rank test $t_{-2\ min}$-$t_{+18\ min}$(DMSO) $p = 0.263$, $t_{-2\ min}$-$t_{+18\ min}$(cytoskeletal inhibitors) $p = 0.041$). **k,** Lumen sphericity before and after treatment (rank-sum test DMSO-cytoskeletal inhibitors $p = 0.003$, Wilcoxon signed rank test $t_{-2\ min}$-$t_{+18\ min}$(DMSO) $p = 0.208$, $t_{-2\ min}$-$t_{+18\ min}$(cytoskeletal inhibitors) $p = 0.099$). **l,** fraction of lumen surface that is concave before and after treatments (rank-sum test DMSO-cytoskeletal inhibitors $p = 0.04$, Wilcoxon signed rank test $t_{-2\ min}$-$t_{+18\ min}$(DMSO) $p = 0.889$, $t_{-2\ min}$-$t_{+18\ min}$(cytoskeletal inhibitors) $p = 0.003$). Scale bars are 10 μm.

Figure 4

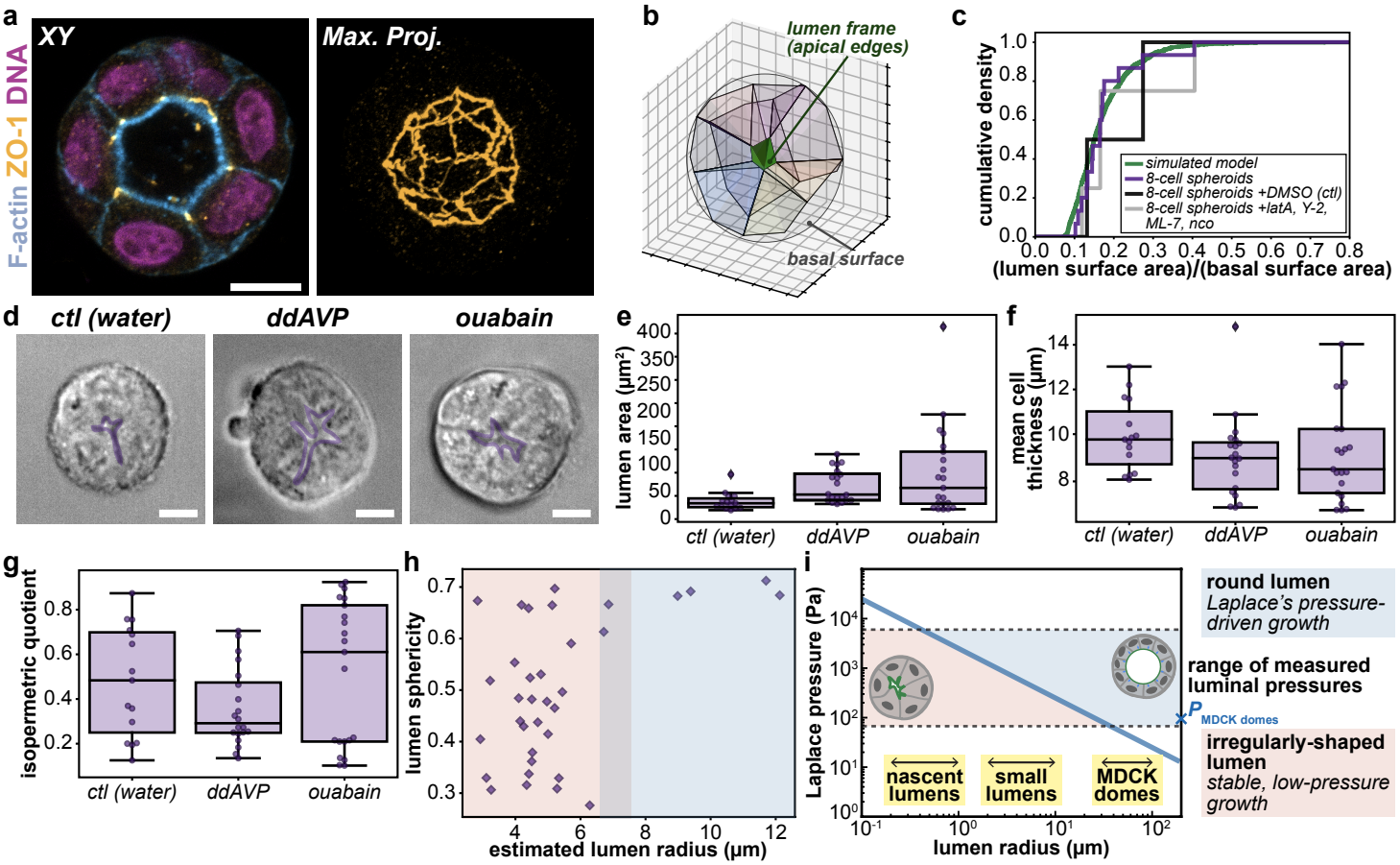

Figure 4 | A cell packing model describes lumen geometry in 8-cell spheroids. a, Representative image of a fixed MDCK spheroid immunostained for F-actin (blue), the apical tight junction protein ZO-1 (orange), and DNA (purple). *XY* slice through the middle of the spheroid (left). Maximum projection in *Z* of the ZO-1 signal (right) **b,** Example random Voronoi packing in an 8-cell spheroid. The spheroid boundary is shown in gray, cell-cell boundaries are in pastel colors, and apical faces are shown in solid green. The random cell-packing model assumes minimal active regulation of lumen surface area or volume and posits that lumen surface area is instead determined by apicobasal (top-bottom) polarization following a random cell-packing. **c,** Cumulative probability distributions for simulated (green) and measured data for lumen surface areas for 8-cell spheroids: untreated spheroids (purple), DMSO vehicle control-treated spheroids (black), and spheroids treated with cytoskeletal inhibitors (latruculin A, Y-27632, ML-7, nocodazole; gray) (see Supplemental Discussion). (2-sample Kolmogorov-Smirnov test model-untreated p = 0.79, model-DMSO p = 0.79, model-drugs p = 0.64). **d,** Representative cross-sections of MDCK spheroids grown for 3 days imaged using differential interference contrast treated with vehicle (top), ddAVP (middle), or ouabain (bottom) for 4 hours. Lumens are outlined in purple. **e,** Quantification of cross-sectional luminal area in control, ddAVP, and ouabain conditions (rank-sum test ctl-ddAVP p = 0.002, ctl-ouabain p = 0.06, ddAVP-ouabain p = 0.1). **f,** Quantification of mean cross-sectional cell wall thickness in control, ddAVP, and ouabain conditions (rank-sum test ctl-ddAVP p = 0.06, ctl-ouabain p = 0.14, ddAVP-ouabain p = 0.87). **g,** Quantification of isoperimetric quoteint of cross-section of lumens in control, ddAVP, and ouabain conditions (rank-sum test ctl-ddAVP p = 0.15, ctl-ouabain p = 0.59, ddAVP-ouabain p = 0.31). **h,** Lumen sphericities plotted as a function of estimated lumen radius. Radius was calculated from lumen volume, if lumen were a perfect sphere. Shading marks transition from irregularly-shaped and more concave lumens (red) to more round and convex lumens (blue). **i,** Proposed transition from irregularly shaped lumens to round lumens. Plot of luminal pressure required to keep lumen open at specified lumen radius, as predicted by Laplace's law (blue line). When lumen size is small, pressure is below the threshold for generating a round lumen (red shading). As lumen size increases the lumen pressure exceeds this pressure and lumen shape and growth is dictated by Laplace's law (blue shading). Scale bars are 10 μm.